Gold Nanoparticles Synthesized from *Fusarium solani* as Efficient Anticancer Agents and Mapping *via* the Fluorescence Staining Technique

Thomas Jerin Sales,[a] Paul Agastian,[b,*] Shine Kadaikunnan,[c] Balamuralikrishnan Balasubramanian,[d] Faisal F. Almutairi,[c] and M. Valan Arasu [c,*]

*Corresponding authors: agastian@loyolacollege.edu; mvalanarasu@ksu.edu.sa

DOI: 10.15376/biores.21.3.6691-6712

GRAPHICAL ABSTRACT

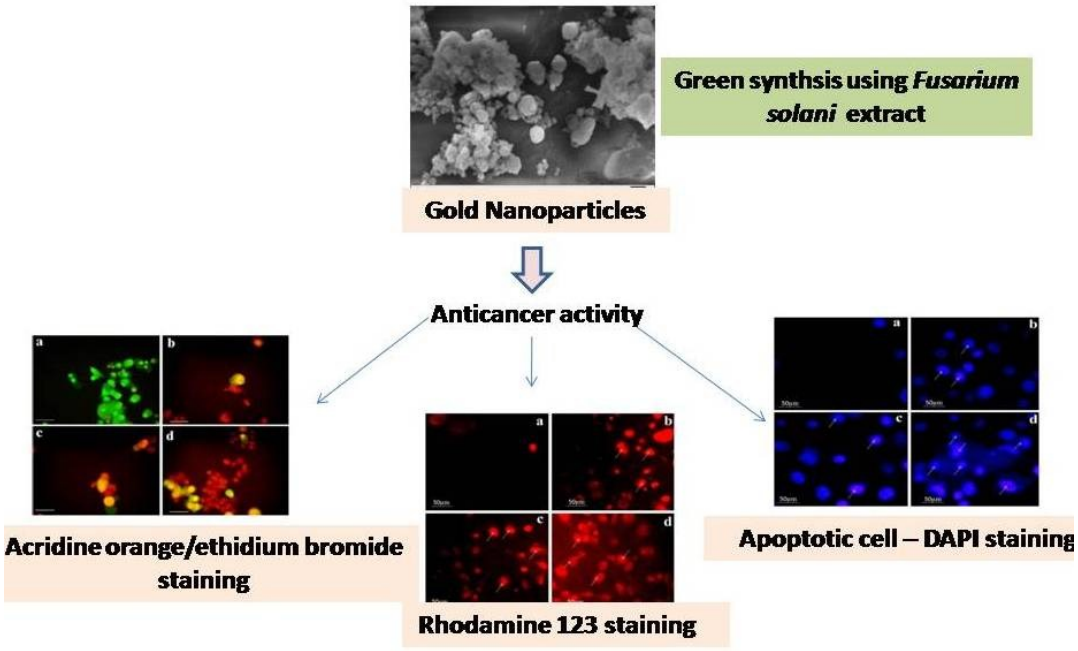

Gold Nanoparticles Synthesized from *Fusarium solani* as Efficient Anticancer Agents and Mapping *via* the Fluorescence Staining Technique

Thomas Jerin Sales,[a] Paul Agastian,[b,*] Shine Kadaikunnan,[c] Balamuralikrishnan Balasubramanian,[d] Faisal F. Almutairi,[c] and M. Valan Arasu [c,*]

The biogenic amalgamation of P-gold nanoparticles (P-AuNPs) was achieved utilizing the unrefined extract of the endophytic organism *Fusarium solani* ATLOY-04 swarmed in *Plumbago rosea*. The synthesized AuNPs were characterized *via* UV–Vis spectroscopy, transmission electron microscopy, and Dynamic light scattering, revealing that 8 to 15 nm nanoparticles were synthesized and were stable. The effects of anticancer cells (MCF-7) on colon cancer (HT-29) and human breast cancer were tested. After the P-AuNPs-treated cells hatched, the MTT test revealed a dose-dependent decrease in cell viability, with the greatest toxicity observed in the cells treated with the Î¼ g/mL and 60 Î¼ g/mL doses of P-AuNPs. The observation of additional apoptotic cells utilizing AO/EtBr, DAPI, and Rhodamine 123 revealed that P-AuNPs initiated apoptosis within the treated cells via atomic fracture, layer breakage, and disturbance of the MMP. Stream cytometry results revealed that cancer cells gathered within the G1 stage after treatment with P-AuNPs, which shows that P-AuNPs affected cancer cell cycle progression. Gold nanoparticles increased the expression of caspase 3 genes and downregulatedp53 protein in MCF-7 cell lines.

DOI: 10.15376/biores.21.3.6691-6712

Keywords: Biosynthesis; Gold nanoparticles; Fusarium solani; Anticancer activity; Apoptosis; Caspase 3; Apoptotic pathway

*Contact information: a: Department of Biotechnology, St. Joseph's College (Arts and Science), Kovur, Chennai 600128, Tamilnadu, India; b: Department of Plant Biology and Biotechnology, Loyola College (Autonomous), Nungambakkam Chennai 600034, Tamilnadu, India; c: Department of Botany and Microbiology, College of Science, King Saud University, P.O. Box 2455, Riyadh 11451, Saudi Arabia; d: Department of Food Science and Biotechnology, College of Life Science, Sejong University, Seoul 05006, South Korea;*Corresponding authors: agastian@loyolacollege.edu;mvalanarasu@ksu.edu.sa*

INTRODUCTION

Owing to their remarkable characteristics and versatile uses, the synthesis and characterization of nanoscale materials have received considerable attention, as have many other classes of materials. Nanoparticles (NPs) are particularly attractive because they exhibit unique and improved mechanical, optical, electrical, magnetic, and catalytic properties and have several applications in biomedical, catalysis, drug delivery, and antimicrobial coatings (Puttasiddaiah *et al*. 2025). Among all the available NPs, gold nanoparticles (AuNPs) are used in several applications, including diagnostics, drug delivery, and cancer treatment. They have been investigated in several cancer therapy clinical trials as drug delivery systems and as diagnostic tools in photothermal therapy, where light is transformed into heat to eradicate cancer cells. Owing to the localized surface

plasmon resonance properties of AuNPs, these materials can be used in biosensors that are capable of identifying specific biomolecules or pathogens and in environmental applications (Ahmed *et al*. 2025). Nanoparticle preparation primarily involves chemical methods in which metal precursors are utilized for the production of NPs by chemical reduction. Nevertheless, owing to increased concern over environmental conservation, the use of green or biological synthesis methods has increased in recent years. Biosynthesis involves the use of microbes such as bacterial culture supernatants, fungal supernatants, plant extracts, and other living organisms and is also referred to as microbe-mediated biosynthesis (Pattnayak *et al*. 2025). This green synthesis method reduces environmental pollution and produces highly stable and bio-compatible NPs. The fungi mediated NPs synthesis has several advantages due to cost-effective production, eco-friendly, superior stability and improved biocompatibility (Aliero *et al*. 2025).

In addition, fungi are rather amenable to culture conditions; they can generate nanosized particles at a relatively large scale in bioreactors. This capability has placed fungi as a resourceful entity in nanotechnology research to produce nanomaterials (Pattnayak *et al*. 2025). In particular, *Fusarium* species are the most preferred fungi for the synthesis of NPs. Biostructured Au NPs, such as those produced by *Fusarium* fungi, have attracted attention because of their anticancer and antimicrobial properties (El-Sharkawy *et al*. 2025). *Plumbago rosea* L. is a medicinal plant which produces a wide range of bioactive compounds and proteins of great interest for endophytic organisms in plant tissues. It produced a wide range of bioactive compounds and proteins of great interest for endophytic organisms in plant tissues (Mukherjee *et al*. 2025). In this work, the potent fungal strain, *Fusarium solani* strain ATLOY-04 was cultivated and the mycelial biomass was used for the synthesis of AuNPs. The green synthesized NPs were characterized and its therapeutic effects on breast cancer cells (MCF-7) and colon cancer (HT-29) cells were analyzed.

EXPERIMENTAL

Materials

Dulbecco's modified Eagle's medium (DMEM), fetal bovine serum (FBS), antibiotics (penicillin and streptomycin), Tris-HCl, EDTA, and acetic acid were procured from Sigma (USA). Agarose and potato dextrose agar (PDA) were purchased from Himedia, India. The P53 primers (5′-AGTCTAGAGCCACCGTCCA-3′ and 5′-TCTGACGCACACCTATTGCAAGC-3′) and Caspase-3 primers (5′-ATGGAGAACA-CTGAAAACTCAGTGGATT-3′ and 5′-CCACCAACCAACCATTTCTTTAGTG-3′) were purchased from Xcelris Labs Ltd., India. Taq 2X master mix and a 100 bp DNA ladder were procured from the companies Amplicon, Denmark, and GeneDirex, USA. The reverse transcription oligo-dT primer was obtained from New England Biolabs(USA). The human breast cancer cell line (MCF-7) was procured from the National Center for Cell Science (NCC), Pune, India.

Isolation of Endophytic Fungi

Fresh leaves of the herb *P. rosea* were used for the isolation of endophytic fungi. The leaves were collected and then washed in running tap water, followed by surface disinfection to reduce the microbial load. The leaves were rinsed with double distilled water and washed with ethanol (70%, 60 s), and sodium hypochlorite solution (2%, 5 min).

The leaves were aseptically ground in a glass homogenizer (Himedia, India). The sample was serially diluted to a 10^{-9} dilution, and 0.1 mL of sample was loaded on PDA medium. The PDA plates were incubated for seven days at 28 °C, and morphologically different fungi were isolated (Rozario *et al*. 2024).

Green Synthesis of Gold Nanoparticles

Morphologically different fungal strains were isolated *via* the single spore method and utilized for the green synthesis of AuNPs prior to molecular characterization. The fungal isolates were cultured in PDA medium and incubated at 28 °C for five days in an orbital shaker incubator at 130 rpm. After five days, the fungal mycelia were harvested by centrifugation (10,000 rpm×10 min) and washed with sterile double distilled water, and the fresh mycelia biomass (intracellular content)was used for the biosynthesis of AuNPs. Freshly collected mycelia (2 g) were mixed with 100 mL of double distilled water and left at room temperature for 48 h. The mixture was filtered, and the filtrate was used for the preparation of AuNPs. A total of 2 mL of fungal biomass suspension was added to a 100 mL aqueous acid chloride solution in an Erlenmeyer flask. The mixture was subsequently placed on a shaker incubator at 130 rpm for 12 h to improve the reduction reaction. The appearance of a reddish color in the flasks indicated the appearance of AuNPs. The color intensity was analyzed, and the fungal strain ATLOY-04, which presented the maximum color intensity, was selected for further studies (Banjara *et al*. 2024). The fungus-mediated biosynthesis of AuNPs is described in Formula 1:

$$\mathrm{AuCl_3} + 2e \longrightarrow \mathrm{AuCl} + 2\mathrm{Cl} - \text{and } 3\mathrm{AuCl} \rightarrow \mathrm{Au_0} + \mathrm{AuCl_3} \quad (1)$$

Molecular Characterization of ATLOY-04

The fungal isolate ATLOY-04 was grown in PDA medium for 20 days at 28 °C. A scalpel was sterilized and scraped from the surface of the PDA plates. The fungal mycelia (250 mg) were freeze-dried and ground finely using a sterile glass homogenizer. The cetyltrimethylammonium bromide (CTAB) method was employed for the extraction of DNA from the mycelia. The ITS1 and ITS4 regions of the strain were amplified *via* universal primers. The amplified PCR product (5 µL) was loaded on a 1% agarose gel containing ethidium bromide (Gupta and Kulkarni 2024). A 100-bp ladder was used to determine the molecular weight of the amplified product. The PCR products were sequenced by Applied Biosystems, and the sequences were deposited in GenBank.

Characterization of P-AuNPs

UV–visible spectroscopy analysis

The development of P-AuNPs was detected from the change in color of the medium from colorless to yellow and then to reddish brown. This color change highlights the presence of P-AuNPs. The absorption spectrum in the range specified for 300 to 800 was used to find the physical features of the biosynthesized P-AuNPs (Ali *et al*. 2024).

Fourier transform infrared spectroscopy analysis

The NPs (5 mg) were finely ground and mixed with potassium bromide (200 mg) and then pressed into a disc (Feng and Ma 2010). The FTIR spectra were acquired by scanning in the range of 400 to 4000 cm^{-1} using an IRTracer-100 spectrophotometer (Shimadzu, Japan). This analysis helps to explore the application of fungal biomass for the

synthesis and stabilization of P-AuNPs. The spectra were acquired by scanning in the range of 400to4000 cm^{-1} using FT-IR spectrophotometry.

X-ray diffraction analysis

The synthesized P-AuNPs were characterized *via* X-ray diffraction with a Regaku Mini Flex 600 instrument equipped with a source of Cu Kα radiation (λ = 1.54 nm). The other working conditions were 40 kV and an electric current of 30 mA at 2θ values of 30–80 (Ruangwicha *et al*. 2024).

Particle size analysis and zeta potential determination

The particle size distribution of the synthesized P-AuNPs was measured *via* a particle size analyzer (Micro politics, Model: Nana Plus). The stability of the NPs was also checked *via* zeta potential (Nithya and Muthumary 2009).

Scanning electron microscopy and energy dispersive X-ray diffraction analysis

To investigate the shape and size of the P-AuNPs, SEM analysis was used. A drop of NPs was placed on the small films and air dried. It was scanned *via* an S-4500 electron scanner. The elemental nature of the NPs was analyzed through EDX analysis (Kumar *et al*. 2013).

High-resolution transmission electron microscopy analysis

The morphology and size of the biosynthesized P-AuNPs were determined using HR-TEM. The sample was prepared by the drop coating method on carbon-coated copper mesh grids after the NPs solution was processed (Burrows *et al*. 2021). The grids were air-dried, and the morphology was examined under a JEOL JEM-2100 electron microscope at 200 kV.

Anti-Cancer Activity

Cell culture

The human breast cancer cell line (MCF-7) and embryonic kidney cells were obtained from the National Centre for Cell Sciences (NCCS), Pune, India. P-AuNPs containing NPs and MCF-7 cells were cultured in DMEM-C (Himedia, India) supplemented with 2 mM L-glutamine, sodium pyruvate, nonessential amino acids,10% fetal bovine serum (FBS) and HEPES buffer (pH 7.2). The IC50 values of the synthesized P-AuNPs were determined in MCF-7 cells (Jiang *et al*. 2007). Antibiotics (10,000 U penicillin/10,000 µg streptomycin) were used to minimize microbial contamination. The cells were maintained in a humidified CO_2 incubator at 37 °C with a CO_2 level of 5% (Balasubramanian *et al*. 2010).

In-vitro cytotoxicity of P-AuNPs

The cytotoxic effect of the P-AuNPs was analyzed *via* the MTT assay. This assay is based on the ability of metabolically active viable cells to convert a substrate into a product that generates a signal proportional to cell viability. The MCF-7 cells (90 µL) (10,000 cells/well) were seeded in 96-well plates supplemented with 0.1% gelatin. The mixture was incubated for 48 h, and 80% confluence was achieved. The media were subsequently changed every 24 h, and fresh media were supplemented with different concentrations of P-AuNPs. After that, the culture medium was replaced, and the cells were incubated for 48 h (Patra *et al*. 2015). The cells were treated with MTT reagent for 4 h at 37 °C, after which viable cells converted this dye to purple formazan crystals. Following

incubation, 100 µL of dimethyl sulfoxide (DMSO) was added to dissolve the formazan crystals, and the absorbance was determined at 620 nm using a microtiter plate reader (ThermoMultiskan EX, USA). The percentage of viable cells was calculated, and the IC50 value was calculated (Wu *et al*. 2019).

Fluorescence microscopic analysis of apoptotic cell death

Acridine orange (AO) and EtBr (100 mg/mL each) fluorescence stains were used to differentiate live cells from apoptotic cells. AO adheres to live and nonviable cells, and EtBr penetrates only nonviable cells, which enables distinguishing between live and apoptotic/necrotic cells. The cells were stained with 100 mg/mL AO or EtBr, incubated for 2 min, and then treated with PBS (Rittenour *et al*. 2012). A fluorescence microscope (Nikon Eclipse, Japan) was then used to analyze the morphological variations in apoptotic cells, including chromatin condensation and fragmentation at 400X magnification, with the use of a 480 nm excitation filter.

4',6-Diamidino-2-phenylindole dihydrochloride (DAPI) nuclear staining

Morphological changes in the nuclei were stained with DAPI to detect apoptosis. DAPI is a blue fluorescence probe that stains the DNA of cells, thus helping to visualize nuclear chromatin condensation, and is the main feature of cell apoptosis. Following 48 h of treatment with P-AuNPs, the MCF-7 cells were fixed with methanol/acetic acid (3:1,V/V). The cells were repeatedly washed with 0.1 M PBS and stained with 1 mg/mL DAPI for 20 min (Akita *et al*. 2013).

Rhodamine 123 staining

The MCF-7 cells were cultured with P-AuNPs for 24 h. The cells were subsequently rinsed with PBS and kept in ice-cold 70% ethanol. The cells were then treated with Rhodamine-123 at a concentration of 5 µg/mL and incubated for 30 minutes at 37 °C. The cells were washed with PBS, and the fluorescein green signal was observed under a microscope. The relative fluorescence intensity of the obtained signals was used to evaluate the membrane potential of the mitochondria and the metabolic activity of the cells. Modifications in mitochondrial function can help predict mitochondrial apoptosis (Sathiyaraj *et al*. 2021).

Cell cycle analysis and phase distribution by flow cytometry

The cell cycle distribution and DNA contents of MCF-7 cells treated with P-AuNPs were determined by flow cytometry. Briefly, the cells (1×10^6) were plated in tissue culture microtiter plates and cultured for 12 h. The adhered cells on the microtiter plates were treated with P-AuNPs for 48 h. Then, the cell lines were trypsinized and immersed in 70% ethanol. The cells were then treated with RNase and finally labeled with the DNA binding dye propidium iodide (PI). The cell cycle phases were determined by the DNA content of the cells from flow cytometry (Dutta *et al*. 2017). These data distinguish the cell cycle at phases where arrest occurs, which is characteristic of many anticancer therapies (Kumar *et al*. 2012).

Expression of p53 and Caspase 3

The human breast cancer cells MCF-7 were cultured with P-AuNPs, and the expression of the p53 and Caspase 3 genes was determined (Malarkodi *et al*. 2013). Briefly, MCF-7 cells were cultured in 6-well tissue culture plates at a density of 1×10^6 cells/mL in

a microtiter plate. Serum-starved cells were cultured in 100 µg/mL P-AuNPs in serum-free DMEM and then incubated at 37 °C in a humidified CO_2incubator for 24 h. Total RNA was isolated from the MCF-7 cells *via* the tri-reagent method. For reverse transcription, a Biorobot (Germany) was used to transcribe 1.0µg of total RNA into complementary DNA (cDNA) *via* OligodT primers and reverse transcriptase in a 20 µL reaction mixture. PCR amplification was performed through p53 and Caspase 3 gene primers. The PCR products were identified from agarose gel electrophoresis. The results were compared with those of the control to evaluate p53 and Caspase 3 gene expression (Vinardell 2005).

Statistical Analysis

All experiments were carried out in three independent trials, and the results were computed using the statistical software SPSS (version 17.0), and $P<0.01$ was considered statistically significant.

RESULTS

Characterization of *Fusarium solani* and Gold Nanoparticle Synthesis

The growth of *F. solani* was observed on PDA plates (Fig. 1a). The developed colonies were 19 mm in diameter. The ITS regions were amplified, and the molecular properties were determined through agarose gel electrophoresis (Fig. 1b). The phylogenetic relationships of the ATLOY-04 strain and closely related fungi from the genus *Fusarium* are depicted in Fig. 1c.

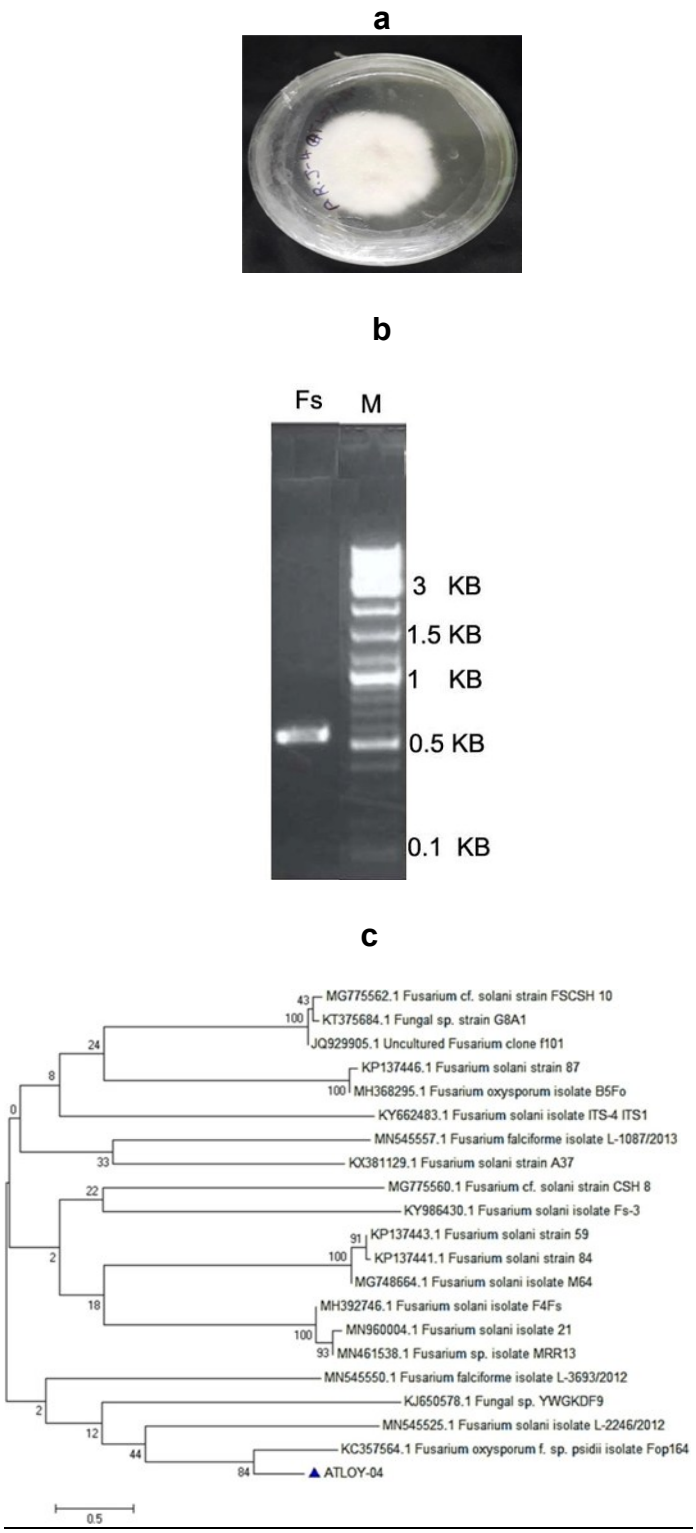

Fig. 1. Growth and molecular characteristics of the endophytic fungus *Fusarium solani*: (a) Growth of *F. solani* on potato dextrose agar medium, (b) 18S rDNA of *F. solani* detected *via* agarose gel electrophoresis, where Lane M represents the DNA ladder and Lane Fs represents the 18S r DNA of strain ATLOY-04, and (c) Phylogenetic relationship of the strain ATLOY-04 and closely related fungi from the *genus Fusarium*

The fungal isolate ATLOY-04 was grown in PDA medium for 20 days at 28 °C. A scalpel was sterilized and scraped from the surface of the PDA plates. The fungal mycelia (250 mg) were freeze-dried and ground finely using a sterile glass homogenizer. The cetyltrimethylammonium bromide (CTAB) method was employed for the extraction of DNA from the mycelia. The ITS1 and ITS4 regions of the strain were amplified *via* universal primers. The amplified PCR product (5 µL) was loaded on a 1% agarose gel containing ethidium bromide (Gupta and Kulkarni 2024). A 100-bp ladder was used to determine the molecular weight of the amplified product. The PCR products were sequenced by Applied Biosystems, and the sequences were deposited in GenBank.

UV–Visible Spectroscopy

This result showed that the P-AuNPs synthesized from *F. solani* presented a unique UV–Visible peak at 540 nm, confirming the development of P-AuNPs. This can be explained by the fact that the color change that occurs during the synthesis process of gold nanoparticles is a result of surface plasmon resonance in the particles. The absorbance peak did not shift and remained at 540 nm throughout the experiment when the incubation time of the fungal extract with gold ions increased (Fig. 2). The consistency of the absorbance peak reveals that there were no significant changes in the structural characteristics of the synthesized P-AuNPs when they are subjected to scanning wavelengths ranging between 300 and 800 nm.

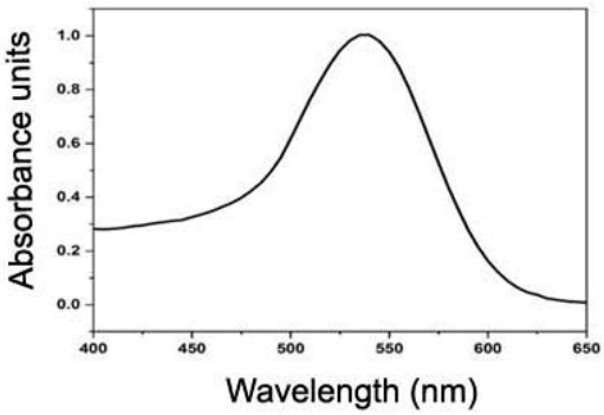

Fig. 2. UV–visible spectrum of P-AuNPs synthesized from the endophyte *Fusarium solani* isolated from *P. rosea*. A major absorption peak was detected at 540 nm.

Fourier Transform Infrared Spectroscopy Analysis of P-AuNPs

The characteristic peaks of the synthesized P-AuNPs were obtained *via* FTIR analysis that identified the bioactive molecules that are responsible for the reduction, capping, and stabilization of the NPs. The FTIR spectra revealed a few characteristic absorption bands regarding the molecular interactions involved in the synthesis of the NPs. The steep absorption band at 3,416 cm^{-1} indicated the stretching vibrations of N–H. Another absorption band was observed at a wavenumber of 1,569 cm^{-1} and represented the bending of N–H, which is common in amines. Furthermore, the bands observed at 1,405 and 1,122 cm^{-1} are attributed to the stretching modes of N–O associated with nitro compounds and the stretching modes of C–N associated with aliphatic amines. The sharp peak observed at approximately 1,405 cm^{-1} was mainly due to the presence of various

amino groups that facilitated the stabilization of P-AuNPs *via* the aqueous extract of *F. solani* (Fig. 3). This peak also corresponds to the reduction of HAuCl to AuNPs, thus supporting the hypothesis that two steps are involved in the synthesis of P-AuNPs: reduction and capping. The FTIR results therefore confirmed that the obtained P-AuNPs exhibited some interaction with the bioactive molecules in the fungal extract required for the synthesis and stabilization of the particles.

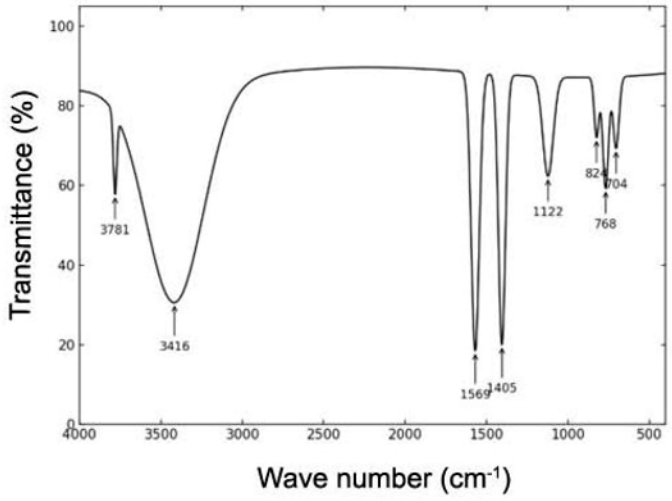

Fig. 3. Fourier transform infrared spectrum of P-AuNPs

X-Ray Diffraction Analysis of P-AuNPs, Particle Size Analysis, and Scanning Electron Microscopy

XRD analysis revealed that four prominent diffraction angles separating at 37.42, 45.90, 64.51, and 77.33 degrees are consistent with the face-centered cubic structures of gold at (111), (200), (220), and (311), respectively. All these peaks indicate that the P-AuNPs were polycrystalline (Fig. 4). The observed XRD pattern was similar to that of the gold nanoparticle patterns. Some other minor peaks may be due to the bioorganic material crystallizing on the nanoparticle surface. The average particle size of the P-AuNPs was 15.1 nm. A total of 85% of the biogenic P-AuNPs possessed a Z-average diameter of 120.6 nm, whereas the PDI value was 0.540, implying a moderate size distribution, and to assess the surface charge and stability of the particles, the ZP was measured. The results of the ZP value indicated that the synthesized P-AuNPs were colloidally stable in suspension (Fig. 5). The size distribution of the P-AuNPs ranged from 10.0 to 40.0 nm, and the mean particle size was 18.2 nm. SEM micrographs provided evidence of the absence of nanoparticle aggregation owing to the presence of capping agents that acted to immobilize the particles. These results further supported the synthesis of gold nanoparticles with specific sizes and shapes (Fig. 6).

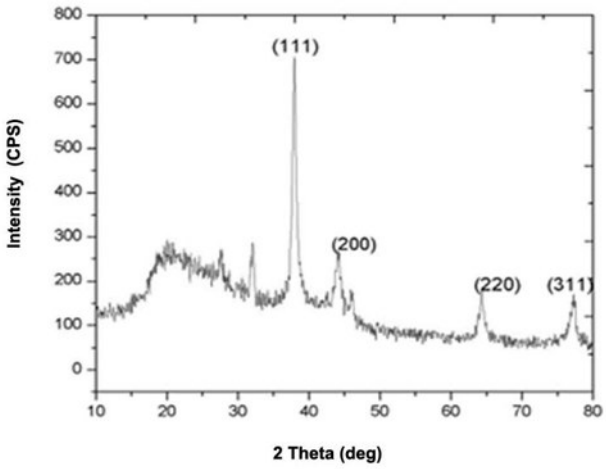

Fig. 4. XRD analysis of green synthesized P-AuNPs

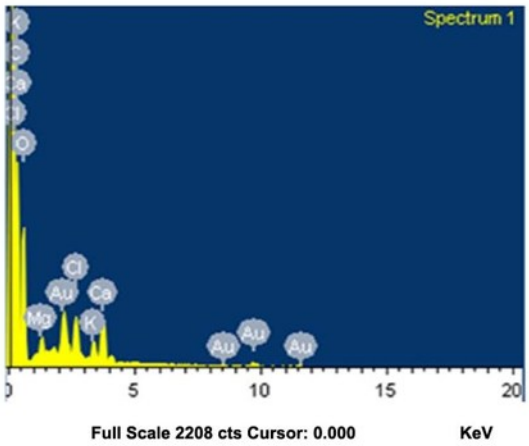

Fig. 5. Particle size analysis of green synthesized P-AuNPs

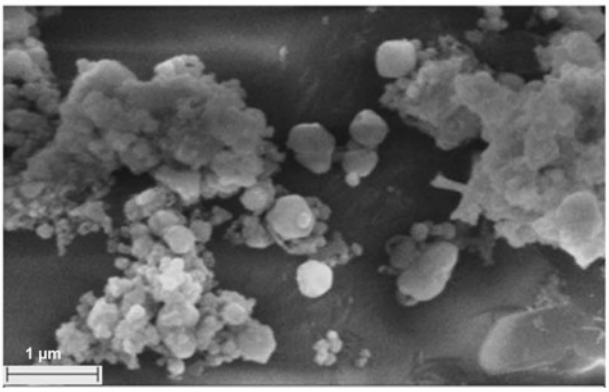

Fig. 6. Scanning electron microscopy analysis of green synthesized P-AuNPs

High-Resolution Transmission Electron Microscopy and EDX Spectrum of the P-AuNPs

The EDX spectrum of the P-AuNPs revealed three signals with peak intensities at 3.1, 8.7, and 11.68 keV, which were assigned to the gold signal (Au). Furthermore, signals for other elements, including carbon (C), calcium (Ca), chlorine (Cl), oxygen (O),

magnesium (Mg), and potassium (K), were detected as indicators of the biomolecules from *F. solani* utilized in the synthesis process (Fig. 7a). HR-TEM provided an accurate picture of the morphological and structural details of the synthesized gold NPs. The NPs were mainly monodispersed, and the detected particle size was approximately 15 nm, although some were in the size range of 8.14 to 18.2 nm (Fig. 7b). Lattice fringes on the surface of the NP scan were observed from HR-TEM as 0.23 nm in size on the basis of the distance between the two consecutive planes, which are the 111 planes of the crystalline lattice of gold. The SAED pattern revealed two distinct circular regions specified as the (200) and (220) planes of the FCC crystalline lattice of gold, which supports the crystalline structure of the biogenic gold nanoparticles (Fig. 7c and d). .

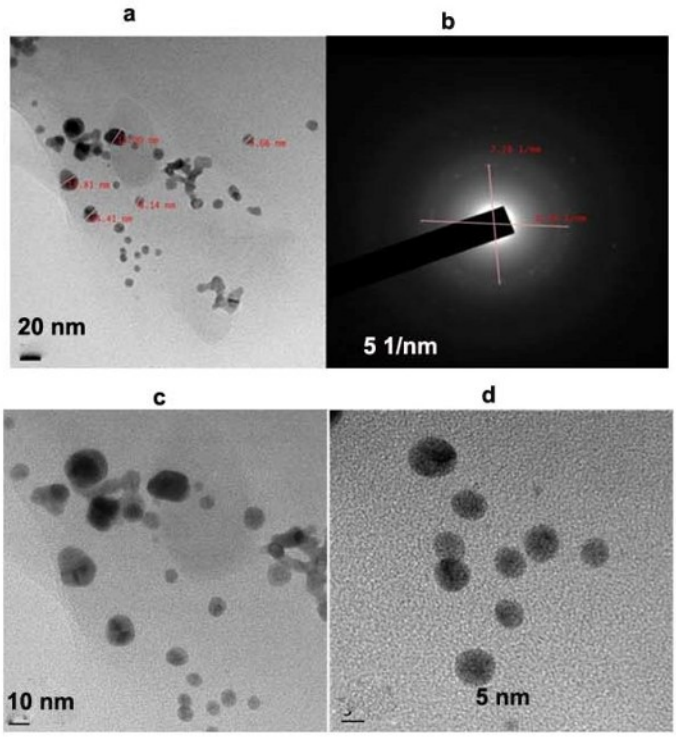

Fig. 7. EDX imaging of green synthesized NPs (a): detection of peak intensities, b: morphological and structural profile of the synthesized gold NPs; c and d: transmission electron microscopy analysis of green synthesized P-AuNPs at two different dimensions.

Cytotoxicity Assay

The cytotoxicity of the synthesized P-AuNPs showed concentration-dependent inhibition of cell proliferation in MCF-7 cells treated with different concentrations of P-AuNPs ranging from 10 to 50 µg/mL. As depicted in Fig. 8, the IC50 values for P-AuNPs were 9.5 ± 0.5 µg/mL for MCF-7 cells and 10.5 ± 0.5 µg/mL for HEK cells. The results revealed that the P-AuNPs were highly cytotoxic to breast cancer cells. In control untreated MCF-7 and HEK293 cells, the cells were closely packed and spindle-shaped, whereas in cells treated with P-AuNPs, growth was severely inhibited, and most cells exhibited irregular membrane blabbing, a manifestation of apoptotic activity (Fig. 9).

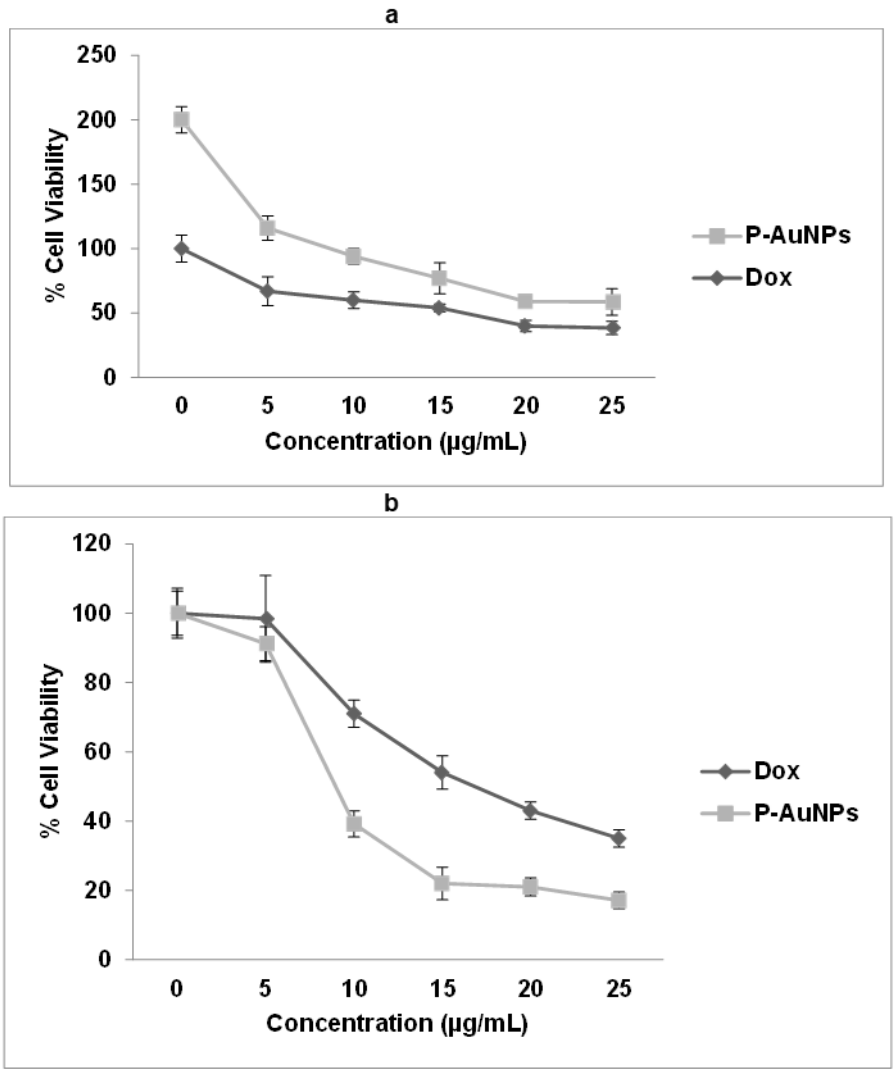

Fig. 8. Percentage cell viability of human breast cancer cell lines (a) and human embryonic kidney cells (b)

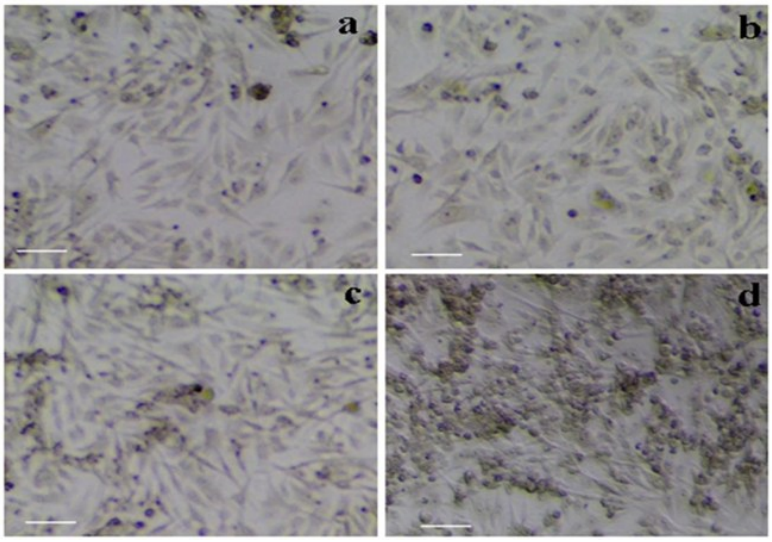

Fig. 9. Cytotoxicity assay - Membrane blebbing, an indicator of apoptosis, was observed in MCF-7 cells treated with P-AuNPs at concentrations ranging from 20, 40, and 60 µg/mL, whereas control cells presented intact membranes.

Acridine Orange/Ethidium Bromide Staining

The apoptotic activity of P-AuNPs was determined by AO/EtBr staining (Fig. 10). The cells treated with P-AuNPs presented characteristic apoptotic features. In the control untreated cells, the orange/red fluorescence was strong, indicating that apoptosis and nuclear condensation were induced by the NPs. The stain differentiated living cells from those undergoing early or late apoptosis. The fluorescence intensity decreased as the progression of apoptosis proceeded. These findings affirm the potential of P-AuNPs to induce apoptosis in MCF-7 cancer cells.

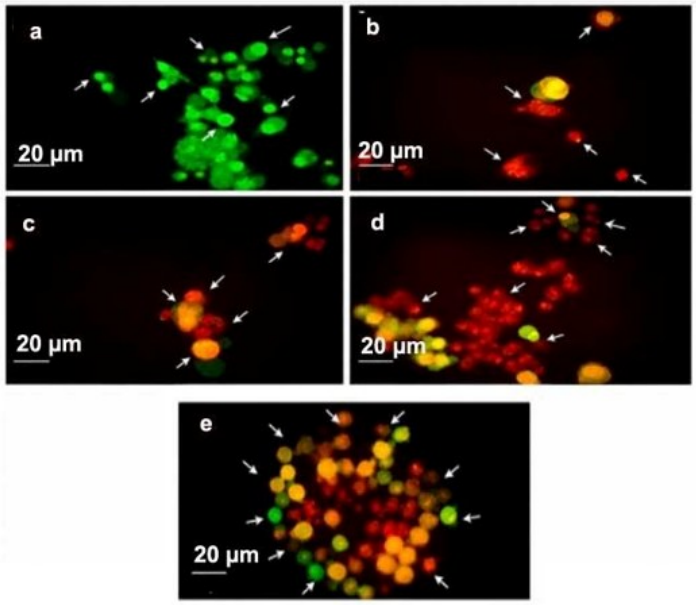

Fig. 10. Acridine orange/ethidium bromide (AO/EtBr) staining is EtBr staining. MCF-7 cells were treated with P-AuNPs at concentrations of 60 (b), 20 (c), and 40 µg/mL (d), and the control (a) highlighted green-colored viable, red-colored necrotic cells, and orange-colored apoptotic cells, while arrows marked the apoptotic cells.

DAPI Staining

Under fluorescence microscopy, as depicted in Fig. 11, cells treated with P-AuNPs presented pronounced nuclear fragmentation and bright fluorescence, indicating chromatin condensation. Cellular nuclei did not show marked changes in the untreated control. These results indicate that the P-AuNPs were potent at inducing nuclear fragmentation in MCF-7 cells.

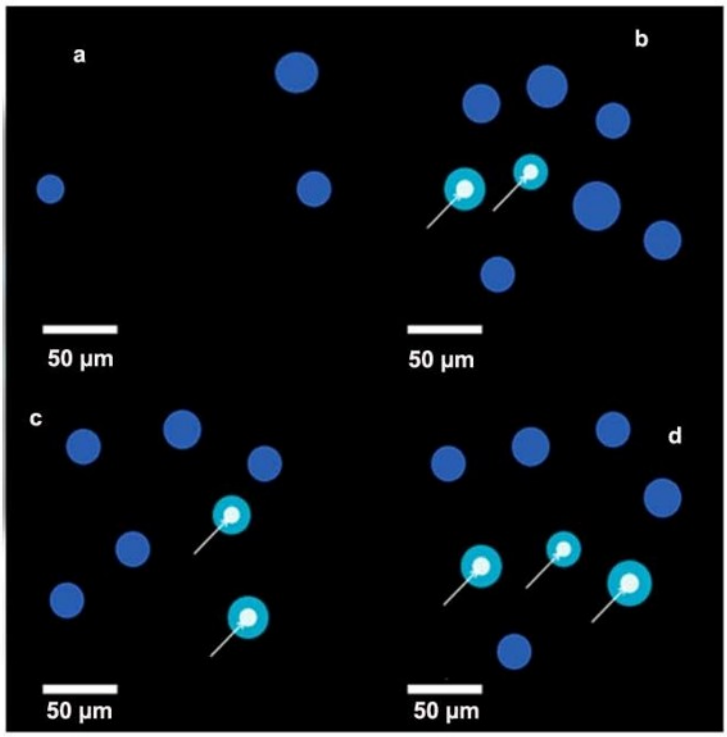

Fig. 11. DAPI staining method for the determination of viable and apoptotic cells at various concentrations of P-AuNPs: a: Control, b: 5 µg/mL; c: 10 µg/mL; and d: 20 µg/mL gold nanoparticles. The arrow indicates the apoptotic cells on the nuclei of the specific cells. The image shows the number of overall cells that survived death in each treatment.

Rhodamine 123 Staining

This staining method was used to determine the effect of P-AuNPs on the mitochondrial membrane potential, which fluoresces red in healthy cells with high membrane potential. The fluorescence intensity decreased in MCF-7 cells after treatment with P-AuNPs, revealing a loss in the mitochondrial membrane potential and a shift toward apoptosis. The fluorescence of the cells exposed to different concentrations of P-AuNPs (5 µg/mL, 10 µg/mL, and 20 µg/mL decreased, indicating the presence of a decreased mitochondrial transmembrane potential along with apoptotic cell death, as shown in Fig. 12. The results thus revealed the effectiveness of P-AuNPs as inducers of cancer cell apoptosis through the loss of mitochondrial membrane integrity.

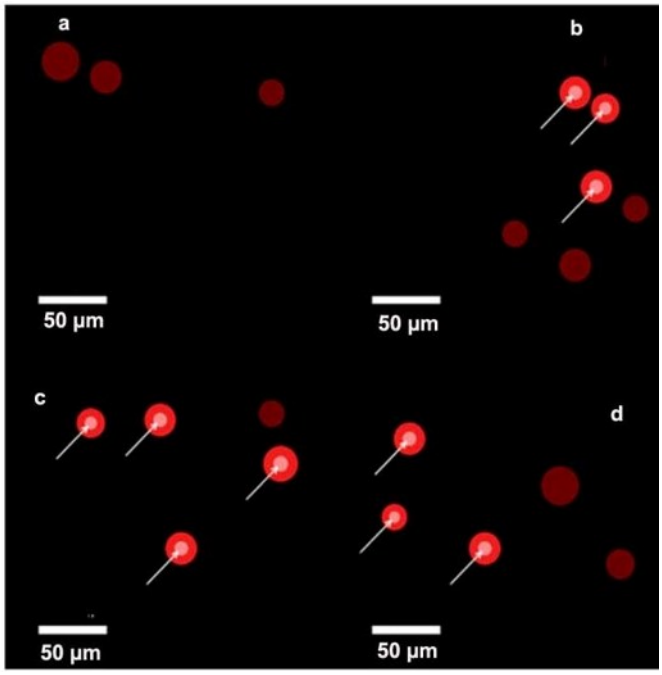

Fig. 12. Staining of viable and apoptotic breast cancer cells treated with various concentrations of gold nanoparticles with rhodamine 123: (a) Control; (b)5 µg/mL; (c) 10 µg/mL; and (c) 20 µg/mL gold nanoparticles. This analysis revealed the ratio of overall dead cells to live MCF-7 cells after the different P-AuNP treatments.

Cell Cycle Arrest

The untreated control cells accumulated at the G0–G1, S, and G2–M phases of the cell cycle. However, cell cycle progression was highly disrupted after treatment with P-AuNPs. Although the percentage of cells in the G0–G1 phase did not vary, the cells that accumulated in the sub-G0 phase were indicative of apoptosis. Compared with those in the control group, the percentages of apoptotic cells in the sub-G0 phase were 60.7%, 53.0%, and 22.5% following treatment with 5, 10, and 20 µg/mL P-AuNPs, respectively (Fig. 13). These studies indicated that P-AuNPs cause cell cycle arrest and induce apoptosis, mainly at the G1 phase, through the inhibition of cyclin expression, leading to a block in the transition from the G1 phase to the S phase of the cell cycle.

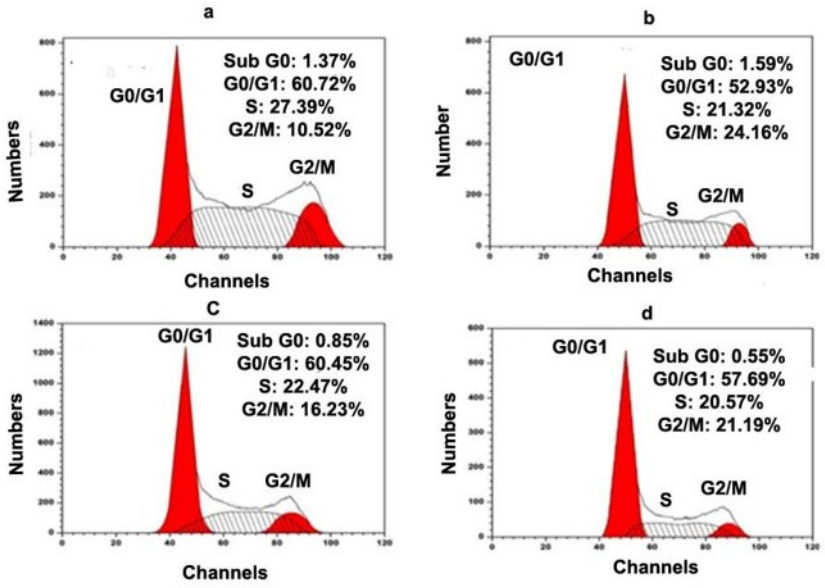

Fig. 13. Cell cycle distribution analysis determined by flow cytometry showing the percentages of cells in Sub G0, G0/G1, S, and G2/M phases. (a) Control cells exhibiting normal cell cycle progression. (b) Cells treated with sample/extract 1 showing increased accumulation in the G2/M phase. (c) Cells treated with sample/extract 2 demonstrating moderate cell cycle arrest with altered S-phase population. (d) Cells treated with sample/extract 3 showing changes in G0/G1 and G2/M populations compared with the control. Histograms represent DNA content measured as channel intensity versus cell number.

Gene Expression Analysis by RT–PCR

The expression of the p53 and Caspase 3 genes in MCF-7 apoptotic cells was detected, and the results are depicted in Fig. 14. The increase in the level of Caspase 3 expression reflected the intrinsic pathway of apoptosis. On the other hand, the p53 protein, a typical tumor-suppressor gene that plays a role in DNA repair, and cell cycle regulation were downregulated in cells treated with P-AuNPs compared with those in the control group. Therefore, these studies revealed that P-AuNPs may stimulate apoptosis in MCF-7 cells *via* the caspase pathway, but if p53 is diminished, the cells cannot respond appropriately to apoptosis, as shown by RT–PCR analysis.

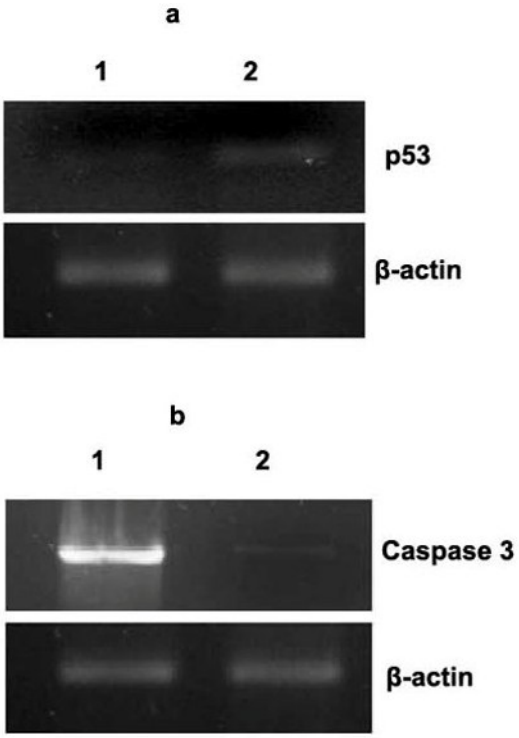

Fig. 14. Expression of the Caspase 3 (a) and P53 (b) genes in breast cancer cell lines. β-Actin was used as the positive control.

DISCUSSION

The color of the synthesized P-AuNPs changed from pale white to reddish-brown, which is a characteristic feature of the formation of AuNPs. This change in color results from a change in the valence state of gold from gold ions (Au^{+}) to elemental gold (Au^{0}) and is typical of what occurs in NPs due to surface plasmon resonance (SPR). The UV–visible spectra of the synthesized P-AuNPs were acquired in the range of 300 to 800 nm. Notably, the absorbance maximum of gold nanoparticles ranges between 525 and 555 nm (Pratheeshkumar *et al*. 2012), which is similar to the results of the present study. In this study, a sharp absorption peak was detected at 540 nm, which was characteristic of the presence of AuNPs. Characterization of P-AuNPs with FTIR revealed the functional properties of the biomolecules responsible for the reduction of gold ions and capping of gold NPs. A very broad band was observed in the range of 3416 cm^{-1}, which was mainly due to the stretching vibrations of N–H groups, which are characteristic of amines and amides. The data obtained in this study indicated that proteins used together with other biomolecules in the filtrate contribute to the reduction of gold ions as well as the stabilization of the NPs. The proteins and peptides from the fungus not only reduced the amount of gold ions but also prevented the NPs from forming large aggregates (Molnár *et al.* 2018). XRD analysis revealed four prominent diffraction angles and is consistent with the face-centered cubic structures of gold NPs. These results agree with the fact that the synthesized gold NPs have a crystalline structure. The shapes of characterized peaks are similar with the common diffraction peaks of gold and further confirm the crystalline nature of the synthesized NPs. The functional gold NPs were prepared earlier, and the fungal filtrate produced crystalline NPs (Gupta and Bector 2013).

SEM images indicated that the primary morphologies of the P-AuNPs were spherical with some aggregation. The size of the resulting NPs was in the range of 8 to 15 nm, and the obtained range in this study commonly exhibited bioactivity (Soltani Nejad *et al.* 2022). TEM images revealed that the nanobeads were spherical to elliptical. The average size of the nanoparticles was found to be approximately 15 nm, with almost negligible agglomeration. This size range is typical of that for nanoparticles synthesized *via* biological routes and agrees with measurements obtained from SEM images. High-resolution TEM images revealed clear lattice fringes on the surface of the NPs, confirming their crystalline nature (Tanaka *et al*. 2016). The diffraction pattern obtained from the XRD analysis revealed the crystallinities of the prepared NPs. EDX spectroscopic analysis revealed the presence of several elements in the NPs. These findings suggest that fungal biomolecules were present together with AuNPs in the treated samples. These elements suggest the biogenesis of P-AuNPs and the integration of fungal biomolecules with the NPs(Ahmed *et al*. 2025). DLS analysis revealed that 85% of the nanoparticles were approximately 120.6 nm in diameter, and the PDI value was 0.540, indicating that these NPs were homogeneous. The zeta potential of the NPs was also determined since it reveals information about their charge density and stability. The present results revealed that the surface charge was moderate in the P-AuNPs, which reduces agglomeration. Cytotoxicity studies of P-AuNPs to MCF-7 breast cancer cells revealed that P-AuNPs were dose dependent, with IC50 values ranging between 10 and 50 µg/mL. Compared with normocytes, green-synthesized NPs were much more cytotoxic to cancer cell lines; therefore, P-AuNPs may be used as selective anticancer agents (Goel *et al*. 2001).

Treatment of cancer cell lines with AO/EtBr followed by fluorescence microscopic examination revealed morphological alterations in the treated cells. These findings suggest that the P-AuNPs induced apoptosis in MCF-7 cells, supporting the possibility of their use as anticancer agents. Moreover, for visualization of DNA damage and confirmation of apoptosis, DAPI staining was performed, which revealed prominent cell shrinkage, rounding, and detachment from the culture plate. To further explore the mechanism of apoptosis, the mitochondrial membrane potential ($\Delta\psi$mit) was evaluated by staining with Rhodamine 123 (RH-123). The results indicated a reduction in the mitochondrial membrane potential caused by P-AuNPs, which is a typical characteristic of apoptosis. The results also revealed that P-AuNPs caused cell cycle arrest at the G1 to S phase transition, which in turn led to the induction of apoptosis in breast cancer cells. The low levels of expression of cyclins also support the concept that P-AuNPs interfere with the cell cycle, causing cells not to progress from the G1 phase into the S phase and therefore reducing proliferation (Mombeini *et al*. 2018).

Gene expression analysis of human breast cancer cells (MCF-7) after treatment with synthesized P-AuNPs supported the hypothesis that the gold NPs had anticancer activity through the induction of apoptosis. The amount of suppressed proliferation and initiated apoptotic pathways in MCF-7 cells depends upon time and dose after being treated with P-AuNPs. The over expression of the caspase-3 and p53 genes is central to the process of apoptosis. Caspase-3 is known as one of the most prominent executioners of caspases in the final stages of apoptosis; it cleaves a variety of cellular substrates, leading to cell death. The P-AuNPs synthesized in the present study progressively induced caspase-3 expression after 24 h and 48 h of treatment, suggesting that the nanoparticles efficiently initiated the apoptotic machinery. The activation of caspase-3, therefore, suggests that the nanoparticles induce apoptosis by activating intrinsic mitochondrial pathways (Yang and Frucht 2001), a process well known to be regulated by caspases. These findings are in line with other

reported findings indicating that gold nanoparticles can stimulate apoptotic signaling in diverse cancer cell lines, such as breast cancer cells. In addition to caspase-3, p53 (a tumor suppressor gene) regulates cell cycle progression and induces apoptosis. The expression of p53 also increased in response to P-AuNP treatment. The upregulation of p53, particularly at 24 h, suggests that it may activate a p53-mediated response to DNA damage or other types of cellular stress with the initiation of apoptosis. The decreased expression of p53 after 48 h could be the result of progression in the apoptotic process or through a feedback mechanism to limit further cell damage (Huang *et al*. 2011).

The upregulation of another key protein involved in the initiation of apoptosis, caspase-9, supports the activation of the mitochondria-mediated pathway (De Robertis 2018). These findings indicate that the synthesized P-AuNPs exerted anticancer effects through disruption of hemostasis between proapoptotic and antiapoptotic factors, initiating mitochondrial dysfunction and activation of caspase cascades that lead to cell death. RT–PCR analysis revealed the induction of the mitochondrial pathway for apoptosis in MCF-7 cells, which is mediated by the synthesis of P-AuNPs. The increased expression of p53 further suggested that these nanoparticles may work through the induction of the p53 pathway in response to oxidative stress and DNA damage. These molecular mechanisms revealed the potential of P-AuNPs as promising therapeutic agents for breast cancer.

CONCLUSIONS

1. The present study reports an eco-friendly, cost-effective method for the green synthesis of gold nanoparticles. In this work, an endophytic fungus, *Fusarium solani* ATLOY-04, which was isolated from *P. rosea,* was used to reduce auric chloride solution, leading to the green synthesis of gold nanoparticles (AuNPs).
2. The synthesized P-AuNPs were characterized *via* UV–Vis spectroscopy, Fourier transform infrared spectroscopy, transmission electron microscopy, dynamic light scattering, and scanning electron microscopy. The synthesized P-AuNPs were ~15 nm in diameter and were found to possess the properties of AuNPs. These nanosized particles exhibited significant activity against human breast cancer cells *in vitro*.
3. The fungal extract of *F. solani* was found to be a promising bioreductant for the synthesis of functionalized AuNPs and has potential for pharmaceutical applications.

ACKNOWLEDGMENTS

The authors express their sincere appreciation to the Ongoing Research Funding Program (ORF-2026-696), King Saud University, Riyadh, Saudi Arabia.

Conflict of interest

We do not have any conflict of interest in publishing this paper.

Use of Generative AI

We did not use any AI tool in the preparation of text, and data analysis.

REFERENCES CITED

Ahmed, Y., Akter, T., Prima, M., Dutta, K. R., Mukut, S., Ahsan, M., Rahman, M. M., and Hyder, M. M. Z. (2025). "Advanced ciprofloxacin quantification: A machine learning and metaheuristic approach using ultrasensitive chitosan-gold nanoparticle based electrochemical sensor," *Journal of Environmental Chemical Engineering* 13(1), article 115094. https://doi.org/10.1016/j.jece.2024.115094

Akita, T., Kohyama, M., and Haruta, M. (2013). "Electron microscopy study of gold nanoparticles deposited on transition metal oxides," *Accounts of Chemical Research* 46(8), 1773-1782. https://doi.org/10.1021/ar300259n

Ali, S. A. B., Abdelmoaty, H., Ramadan, H., and Salman, Y. (2024). "The endophytic fungus *Epicoccum nigrum*: Isolation, molecular identification and study its antifungal activity against phytopathogenic fungus *Fusarium solani*," *Journal of Microbiology Biotechnology and Food Sciences*13(5), e10093-e10093. https://doi.org/10.55251/jmbfs.10093

Aliero, A. S., Hasmoni, S. H., Haruna, A., Isah, M., Malek, N. A. N. N., and Zawawi, N. A. (2025). "Bibliometric exploration of green synthesized silver nanoparticles for antibacterial activity," *Emerging Contaminants*11(1), article 100411. https://doi.org/10.1016/j.emcon.2024.100411

Balasubramanian, S. K., Yang, L., Yung, L. Y. L., Ong, C. N., Ong, W. Y., and Yu, L. E. (2010). "Characterization, purification, and stability of gold nanoparticles," *Biomaterials* 31(34), 9023-9030. https://doi.org/10.1016/j.biomaterials.2010.08.012

Banjara, R. A., Kumar, A., Aneshwari, R. K., Satnami, M. L., and Sinha, S. K. (2024). "A comparative analysis of chemical *vs* green synthesis of nanoparticles and their various applications," *Environmental Nanotechnology, Monitoring and Management* 22, article 100988. https://doi.org/10.1016/j.enmm.2024.100988

Burrows, A., Holman, J., Lancaster, S., Overton, T., Parsons, A., Pilling, G., and Price, G. (2021). *Chemistry 3: Introducing Inorganic, Organic and Physical Chemistry*, Oxford University Press.

De Robertis, M. (2018). "miRNA expression profiling of mouse colon cancer stem cells: A tumor-specific signature traceable along colorectal cancer progression with prognostic value in human colon cancer," *Meta Gene* 17, S10-S11. https://doi.org/10.1016/j.mgene.2018.05.046

Dutta, P. P., Bordoloi, M., Gogoi, K., Roy, S., Narzary, B., Bhattacharyya, D. R., Mohapatra, P. K., and Mazumder, B. (2017). "Antimalarial silver and gold nanoparticles: Green synthesis, characterization and in vitro study," *Biomedicine and Pharmacotherapy* 91, 567-580. https://doi.org/10.1016/j.biopha.2017.04.032

El-Sharkawy, R. M., Ahmed, I. A., and Kharboush, T. G. (2025). "Fusarium oxysporum assisted green synthesis of small-sized silver nanoparticles for high antibacterial, and photocatalytic decolorization performances," *BMC Microbiology* 25(1), article 4. https://doi.org/10.1186/s12866-024-03686-7

Feng, C., and Ma, Y. (2010). "Isolation and anti-phytopathogenic activity of secondary metabolites from *Alternaria* sp. FL25, an endophytic fungus in *Ficus carica*," *Chinese Journal of Applied and Environmental Biology* 16, 76-78.

Goel, A., Boland, C. R., and Chauhan, D. P. (2001). "Specific inhibition of cyclooxygenase-2 (COX-2) expression by dietary curcumin in HT-29 human colon cancer cells," *Cancer Letters* 172(2), 111-118. https://doi.org/10.1016/s0304-3835(01)00655-3

Gupta, S. and Bector, S. (2013). 'Biosynthesis of extracellular and intracellular gold nanoparticles by *Aspergillus fumigatus* and *A. flavus*,' *Antonie van Leeuwenhoek* 103, 1113-1123. https://doi.org/10.1007/s10482-013-9892-6

Gupta, R., and Kulkarni, P. (2024). "Molecular characterization and screening of protease production from indigenous thermophilic fungi *Malbranchea cinnamomea* isolated from dairy farm compost soil," *Annals of Plant and Soil Research* 26(2), 243-249. https://doi.org/10.47815/apsr.2024.10356

Huang, Y. S., Xie, N., Su, Q., Su, J., Huang, C., and Liao, Q. J. (2011). "Diallyl disulfide inhibits the proliferation of HT-29 human colon cancer cells by inducing differentially expressed genes," *Molecular Medicine Reports* 4(3), 553-559. https://doi.org/10.3892/mmr.2011.453

Jiang, G., Wang, L., and Chen, W. (2007). "Studies on the preparation and characterization of gold nanoparticles protected by dendrons," *Materials Letters* 61(1), 278-283. https://doi.org/10.1016/j.matlet.2006.04.110

Kumar, A., Patil, D., Rajamohanan, P. R., and Ahmad, A. (2013). "Isolation, purification and characterization of vinblastine and vincristine from endophytic fungus *Fusarium oxysporum* isolated from *Catharanthus roseus*," *PloS One* 8(9), article e71805. https://doi.org/10.1371/journal.pone.0071805

Kumar, K. M., Mandal, B. K., Sinha, M., and Krishnakumar, V. (2012). "*Terminalia chebula* mediated green and rapid synthesis of gold nanoparticles," *Spectrochimica Acta Part A: Molecular and Biomolecular Spectroscopy* 86, 490-494. https://doi.org/10.1016/j.saa.2011.11.001

Malarkodi, C., Rajeshkumar, S., Vanaja, M., Paulkumar, K., Gnanajobitha, G., and Annadurai, G. (2013). "Eco-friendly synthesis and characterization of gold nanoparticles using *Klebsiella pneumonia*," *Journal of Nanostructure in Chemistry* 3(1), article 30. https://doi.org/10.1186/2193-8865-3-30

Molnár, Z., Bódai, V., Szakacs, G., Erdélyi, B., Fogarassy, Z., Sáfrán, G., Varga, T., Kónya, Z., Tóth-Szeles, E., Szűcs, R. and Lagzi, I. (2018). "Green synthesis of gold nanoparticles by thermophilic filamentous fungi," *Scientific Reports* 8(1), p. 3943. https://doi.org/10.1038/s41598-018-22112-3

Mombeini, M., Saki, G., Khorsandi, L., and Bavarsad, N. (2018). "Effects of silymarin-loaded nanoparticles on HT-29 human colon cancer cells," *Medicina* 54(1), article 1. https://doi.org/10.3390/medicina54010001

Mukherjee, S., Hossain, M.A., Raj, A., Sikdar, B. and Roy, S. (2025). "The antibacterial and antioxidant activities of plumbagin-rich methanolic root extracts from *Plumbago zeylanica* L.," *The Microbe 7*, article 100293. https://doi.org/10.1016/j.microb.2025.100293

Nithya, K., and Muthumary, J. (2009). "Growth studies of *Colletotrichum gloeosporioides* (Penz.) Sacc.-a taxol producing endophytic fungus from *Plumeria acutifolia*," *Indian Journal of Science and Technology* 2(11), 14-19.

Patra, S., Mukherjee, S., Barui, A. K., Ganguly, A., Sreedhar, B., and Patra, C. R. (2015). "Green synthesis, characterization of gold and silver nanoparticles and their potential application for cancer therapeutics," *Materials Science and Engineering: C*53, 298-309. https://doi.org/10.1016/j.msec.2015.04.048

Pattnayak, S., Choudhury, S., and Hota, G. (2025). "Green chemistry mediated and biogenic synthesis of gold nanoparticles: Prospects and challenges," *Gold Nanoparticles, Nanomaterials and Nanocomposites* 81-111. https://doi.org/10.1016/B978-0-443-15897-1.00003-0

Pratheeshkumar, P., Sheeja, K., and Kuttan, G. (2012). "Andrographolide induces apoptosis in B16F-10 melanoma cells by inhibiting NF-κB-mediated bcl-2 activation and modulating p53-induced caspase-3 gene expression," *Immunopharmacology and Immunotoxicology* 34(1), 143-151. https://doi.org/10.3109/08923973.2011.588233

Puttasiddaiah, R., Basavegowda, N., Lakshmanagowda, N. K., Raghavendra, V. B., Sagar, N., Sridhar, K., Dikkala, P. K., Bhaswant, M., Baek, K. H., and Sharma, M. (2025). "Emerging nanoparticle-based diagnostics and therapeutics for cancer: Innovations and challenges," *Pharmaceutics* 17(1), article 70. https://doi.org/10.3390/pharmaceutics17010070

Rittenour, W. R., Park, J. H., Cox-Ganser, J. M., Beezhold, D. H., and Green, B. J. (2012). "Comparison of DNA extraction methodologies used for assessing fungal diversity via ITS sequencing," *Journal of Environmental Monitoring* 14(3), 766-774. https://doi.org/10.1039/C2EM10779A

Rozario, S. J., Khusro, A., Agastian, P., Almutairi, M. H., and Almutairi, B. O. (2024). "Bioassay-guided fractionation and biological activities of antimycin A and 4-hydroxybenzoic acid isolated from *Nocardiopsis* sp. strain LC-9," *BioResources*19(4), 7673-7697. https://doi.org/10.15376/biores.19.4.7673-7697

Ruangwicha, J., Cheirsilp, B., and Suyotha, W. (2024). "Green biorefinery of shrimp shell waste for α-chitin and high-value co-products through successive fermentation by co-lactic acid bacteria and proteolytic fungus," *Bioresource Technology* 393, article 130106. https://doi.org/10.1016/j.biortech.2023.130106

Sathiyaraj, S., Suriyakala, G., Gandhi, A. D., Babujanarthanam, R., Almaary, K. S., Chen, T. W., and Kaviyarasu, K. (2021). "Biosynthesis, characterization, and antibacterial activity of gold nanoparticles," *Journal of Infection and Public Health* 14(12), 1842-1847. https://doi.org/10.1016/j.jiph.2021.10.007

Soltani Nejad, M., Samandari Najafabadi, N., Aghighi, S., Pakina, E. and Zargar, M. (2022). "Evaluation of *Phoma* sp. biomass as an endophytic fungus for synthesis of extracellular gold nanoparticles with antibacterial and antifungal properties," *Molecules* 27(4), article 1181. https://doi.org/10.3390/molecules27041181

Tanaka, R., Tomosugi, M., Sakai, T., and Sowa, Y. (2016). "MEK inhibitor suppresses expression of the miR-17-92 cluster with G1-phase arrest in HT-29 human colon cancer cells and MIA PaCa-2 pancreatic cancer cells," *Anticancer Research* 36(9), 4537-4543. https://doi.org/10.21873/anticanres.11001

Vinardell, M. P. (2005). "*In vitro* cytotoxicity of nanoparticles in mammalian germ-line stem cell," *Toxicological Sciences* 88(2), 285-286. https://doi.org/10.1093/toxsci/kfi340

Wu, B., Hussain, M., Zhang, W., Stadler, M., Liu, X., and Xiang, M. (2019). "Current insights into fungal species diversity and perspective on naming the environmental DNA sequences of fungi," *Mycology* 10(3), 127-140. https://doi.org/10.1080/21501203.2019.1614106

Yang, W. L., and Frucht, H. (2001). "Activation of the PPAR pathway induces apoptosis and COX-2 inhibition in HT-29 human colon cancer cells," *Carcinogenesis* 22(9), 1379-1383. https://doi.org/10.1093/carcin/22.9.1379

Article submitted: December 12, 2025; Peer review completed: March 19, 2026;
Revisions accepted: May 22, 2026; Published: June 5, 2026.
DOI: 10.15376/biores.21.3.6691-6712